AIAA JOURNAL
Vol. 46, No. 3, March 2008

Time-Domain Spectral Element Method for Built-In Piezoelectric-Actuator-Induced Lamb Wave Propagation Analysis

Yujun Kim,* Sungwon Ha,† and Fu-Kuo Chang‡
Stanford University, Stanford, California 94305

DOI: 10.2514/1.27046

An investigation was performed to develop a computational model based on a spectral element method to simulate piezoelectric-actuator-induced acousto-ultrasonic wave propagation in a metallic structure. The model solves the coupled electromechanical field equations simultaneously in both three-dimensional and two-dimensional plane strain conditions, and so it can accept any arbitrary waveform of electrical voltage as input to any piezoelectric transducer and produce piezoelectric sensor output in voltage as a result of the excitation generated by the transducer. Basically, the model inputs electrical voltage to actuators and outputs electrical signals of sensors. To visualize the transient dynamic wave motions in the structure generated by the transducer, the code is integrated with commercial pre/postprocessing software to provide graphical outputs of the dynamic deformations of the structure. The code was verified by comparison with experimental results. Performance of the model was examined in terms of solution convergence compared with the finite element method.

Nomenclature

D_i	=	electric displacement vector components
E_i	=	electric field vector components
ε_{ij}	=	strain tensor components
F_i^{ext}	=	external force vector components
F_i^{int}	=	internal force vector components
h_q	=	1-D Lagrange interpolations
K_{ij}	=	dielectric stiffness tensor components
$\hat{K}_{ij}$	=	piezoelectric stiffness tensor components
M_{ij}	=	X component of the resultant pressure force acting on the vehicle
Q	=	electric charge
t_i	=	time index during navigation
u_i	=	displacement vector components
$\ddot{u}_j$	=	acceleration vector components
V	=	electric potential
ρ	=	density
σ_{ij}	=	stress tensor components

I. Introduction

THE use of acousto-ultrasound technology for built-in transducers (actuators and sensors) in structural health monitoring has made significant progress recently through demonstrations of real-time inspection and damage detection [1–4]. A key feature for detecting damage from these built-in actuators and sensors is the use of the wave scatter, which is a comparison of waveforms of sensor signals induced by the actuators before and after the introduction of damage [3,4]. The wave scatters are easy to produce in experiment, but they are very difficult to simulate accurately. A fundamental understanding of these wave scatters generated in these structures is crucial for developing adequate diagnostic algorithms for interpreting the sensor signals in terms of damage location and size.

To accurately catch the wave scatters, any analytical or numerical model must not only be able to accurately simulate the wave propagation in terms of waveform (phase and amplitude) induced by the actuators and measured by the sensors, but must also take into account the dynamic interface interaction between the actuator/sensor and the host structure. Numerical methods such as the finite element method (FEM), the finite difference method, and the boundary-element method have been employed to study how these Lamb waves behave in structures and interact with defects [5–10]. A common feature of these numerical methods is abbreviated to time and spatial discretizations. These approximations induce inherent errors in the numerical solution in phase and amplitude. In the case of ultrasonic wave propagation, the major numerical challenge is to minimize numerical dispersion error [11]. If the error of phase and group velocities resulting from the numerical dispersion is accumulated through time and space, the resulting wave scatters would yield very different solutions from the real situation, resulting in useless information. Therefore, the success of numerical analysis strongly depends on minimization of the error, which requires sufficient discrete spatial resolution per minimum wavelength.

FEM, which is one of the most efficient simulation techniques for obtaining a solution to wave-propagation problem in structures, has served as a primary computational tool for understanding stress wave propagation and its scatter at inhomogeneities. Use of the FEM has been encouraged by competitive advantages for modeling of geometrical complexity, material anisotropy, and a traction-free boundary condition, when compared with the finite difference and boundary element methods. However, from a practical viewpoint, the diagnostic Lamb waves employed to detect damage in platelike structures have less than several millimeters as a minimum wavelength. In the case of even nonguided waves, explicit FEM requires more than 20 elements per minimum wavelength to obtain a solution with a less than 1.0% dispersive error [11]. Thus, finite element analysis for guided wave propagation requires spatial discretizations of less than a few tenths of a millimeter to compute an accurate solution. It follows that FEM for three-dimensional problems would require impractical computational resources, such as computing time and memory. This is the main reason practical use of FEM in the field of Lamb wave-based simulations has severe restrictions and limitations.

The spectral element method (SEM) in the time domain is an alternative to the existing numerical methods in the field of Lamb wave-based structural health monitoring. The SEM first developed in the mid 1980s [12] is a weighted residual method, like FEM. The main features of the SEM are a subdivided whole domain, called elements, and high-order interpolation with particular quadrature

Received 7 August 2006; accepted for publication 14 October 2007.

*Research Associate, Department of Aeronautics and Astronautics; yujun@stanford.edu.
†Research Assistant, Department of Aeronautics and Astronautics; swha1@stanford.edu.
‡Professor, Department of Aeronautics and Astronautics; fkchang@stanford.edu. Fellow Member AIAA.

rules. SEM by use of the Legendre formulation shows an important numerical feature to diagonalize inertia terms, which results in far fewer arithmetic operations. Furthermore, the SEM has an exponential rate of solution convergence and conserves the aforementioned advantages of FEM, which significantly enhances the capability to simulate wave propagation [13]. Consequently, numerical analysis by use of the SEM leads to drastic reduction of the required computational resources. The fields of acoustics and seismology have enjoyed the advantages of the SEM [14–17]. Recently, SEM in the frequency domain has been introduced to damage-detection technology [18] by use of the Fourier synthesis of many infinitely long wave trains of different frequencies [19]. However, in the context of computational efficiency, time-domain analysis for wave propagation is intrinsically a better choice. Thus, in this paper, the SEM in the time domain is proposed for modeling the Lamb wave propagation in structures with a network of built-in piezoelectric actuators and sensors.

Because wave scatters are affected strongly by the interfacial interaction between the actuator/sensor and the host structure, the SEM model must consider the dynamic piezoelectric effects of actuators and sensors to the host structure. Therefore, a spectral element formulation in the time domain will be discussed, based on the coupled electromechanical equations for piezoelectric material. As a solution procedure for the coupled equation, the simultaneous employment of an explicit time-integration scheme for the semidiscrete dynamic equations and Gauss elimination method for the static electric field is presented. Furthermore, as a pre/postprocessor to grant access to the geometrical complexity of host structures, an interface program that links to well-known commercial CAD/CAE code was developed. The interface programs automatically transfer the generated finite element data into spectral element data, and vice versa.

II. Spectral Element Formulation

In the same way as the FEM, the SEM is an approximation method called the weight residual method [20]. In a fixed rectangular Cartesian coordinate system, let σ_{ij}, u_j, $\ddot{u}_j$, D_i, and ρ be the stress, displacement, acceleration, electric displacement, and density, respectively. Then, on the basis of the physical equation of equilibrium, the strong form of the boundary-value problem known to govern the behavior of a host structure with piezoelectric sensors is stated as follows [21]:

For equilibrium equations,

$$\sigma_{ij,i} = \rho \ddot{u}_j \quad \text{in } \Omega^{S+P} \qquad D_{i,i} = 0 \quad \text{in } \Omega^{P} \tag{1a}$$

For boundary conditions,

$$\begin{aligned} u_i &= \bar{u}_i \quad \text{on } S_u^{S+P} \qquad \sigma_{ij} n_i = \bar{t}_j \quad \text{on } S_t^{S+P} \\ V &= \bar{V} \quad \text{on } S_V^{P} \qquad D_i n_i = Q \quad \text{on } S_Q^{P} \end{aligned} \tag{1b}$$

where superscripts S and P mean the domain of the host structure and piezoelectric sensors, respectively. Furthermore, subscripts u, t, V, and Q indicate surfaces prescribed by displacement, traction, electric potential, and electric charge, respectively. Summation is implied on the repeated indices unless stated otherwise, and a comma indicates partial differentiation with respect to the coordinate direction. Hereafter, under the assumption of the three-dimensional problem, the lower case indices i, j, and k are used to indicate the directions 1, 2, and 3.

Based on the principle of virtual work, the spectral element formulation evolves from transformation of the strong form [Eqs. (1a) and (1b)] into the weak form, called weight residual formulation [21]:

$$\begin{aligned} &\int_{\Omega^{S+P}} (\sigma_{ij}\delta\varepsilon_{ij} + \rho \ddot{u}_i \delta u_i)\, \mathrm{d}\Omega - \int_{\Omega^{P}} D_i \delta E_i \, \mathrm{d}\Omega \\ &\quad = \int_{S_t^{S+P}} \bar{t}_i \delta u_i \, \mathrm{d}S + \int_{S_Q^{P}} Q \delta V \, \mathrm{d}S \end{aligned} \tag{2}$$

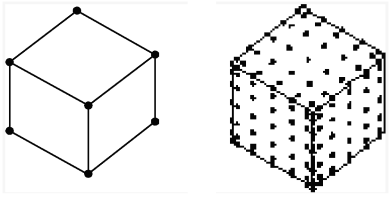

a) b)

Fig. 1 Comparison between a) linear finite element and b) sixth-order spectral element.

To transfer this weak form into the spectral element equation, the same procedures that formulate a typical finite element equation are followed: The whole domain is subdivided into many small subdomains called elements, and then low-order interpolation functions and Gauss quadrature rules are applied to the element. Contrary to the classical finite element approximation, the SEM approximates the field variables in elements using a high-order one-dimensional Lagrange polynomial and its tensor product. For example, the displacement vector can be written as follows [17]:

$$u_i(\xi, \eta, \zeta) = \sum_{p=0}^{N} \sum_{q=0}^{N} \sum_{r=0}^{N} h_p(\xi) h_q(\eta) h_r(\zeta) d_i^{pqr} \tag{3}$$

where ξ, η, and ς indicate a local coordinate system, and $h_p(\xi)$ is an Nth-order 1-D Lagrange interpolation function at $(N+1)$ Gauss–Lobatto–Legendre (GLL) points [17], which show uneven distribution of nodal spaces (see Fig. 1). Use of the Gauss–Lobatto–Legendre quadrature leads the integral Eq. (2) to the coupled spectral element equations, which means mechanical force and electrical charge equilibrium at each node:

$$M_{ij} \ddot{d}_j = F_i^{\text{ext}} - F_i^{\text{int}} \quad \text{in } \Omega^{S+P} \tag{4a}$$

$$\hat{K}_{ij} d_j - K_{ij} \phi_j = P_i \quad \text{in } \Omega^{P} \tag{4b}$$

where M_{ij} is the lumped mass matrix , $\ddot{d}_j$ the is acceleration vector, and F_i^{ext} and F_i^{int} are external and internal force vectors, respectively. In the static equilibrium Eq. (4b), d_j and ϕ_j are nodal displacement and electric potential vectors. Furthermore, P_i is electric charge vector, and $\hat{K}_{ij}$ and K_{ij} are the piezoelectric stiffness matrix and the dielectric stiffness matrix, respectively.

Because of Legendre formulation, the mass matrix in Eq. (4a) leads to a naturally diagonal matrix. Furthermore, in the context of features for wave propagation, the explicit time-integration scheme, such as the central-difference method, is the best choice for calculating the ordinary differential equation (4a) in the time domain. As a strategy for solving the coupled equations (4a) and (4b) simultaneously, in each time step, the mechanical fields such as acceleration, velocity, displacement, and stress are estimated on the basis of electric potential and mechanical fields obtained from the previous time step. Then using the estimated displacements and the Gauss elimination algorithm, the static equation for the electric field [Eq. (4b)] provides the new electric potentials at the current time step. At the next time step, the obtained displacements and electric potentials are used again as the field variables of the previous time step. All these procedures are iterating to the end-time step.

III. Model Verification

The experiment was conducted on a square aluminum-alloy plate (thickness of 1.02 mm and width and height of 508 mm), as shown in Fig. 2a, to validate the proposed SEM model. Four identical piezoelectric transducers were mounted on one side of the plate, as shown in Fig. 2a. Table 1 shows the locations of the piezoelectric transducers on the plate. The electromechanical properties of the piezoelectric materials (APC850) are available from American

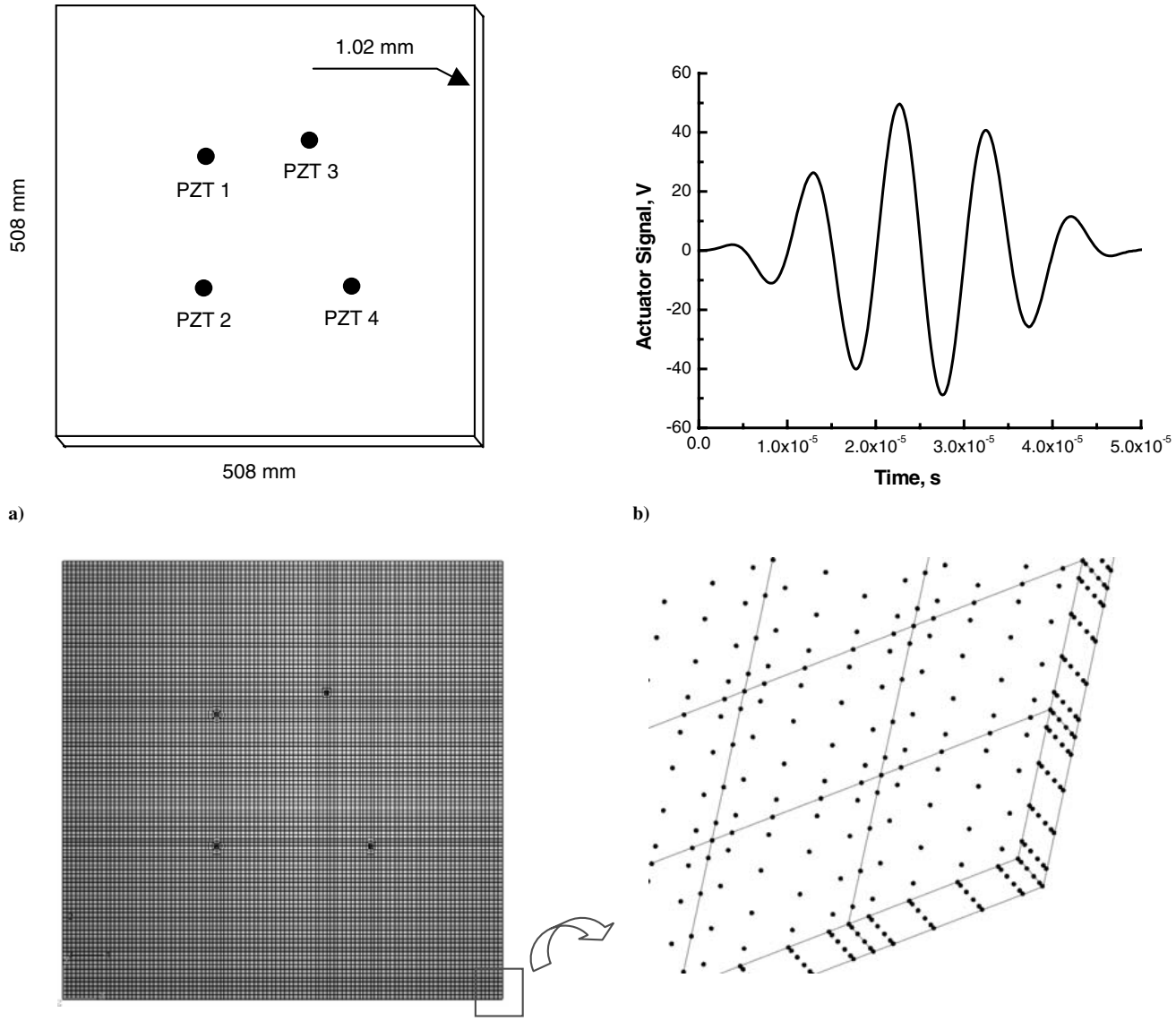

Fig. 2 Square aluminum plate with four piezoelectric transducers on one side a) geometric configuration, b) excitation signal (100 kHz) at PZT 2, and c) mesh configuration elements and nodes.

Piezoceramics, Inc. The piezoceramic element used is a disk with 0.25-mm thickness and 6.35-mm diameter. The experiment was made using a pitch–catch setup, in which one of the transducers acted as an actuator to generate Lamb waves and the other transducers received the propagating Lamb waves. The peak voltage of the excitation was kept at 50 V. In the experiment, PZT 2 as an actuator excited a five-peak tone-burst wave with a center frequency of 100 kHz, as shown in Fig. 2b. According to Lamb's wave dispersion equation [3,4], at this frequency–thickness value, there are only fundamental symmetric and antisymmetric modes, due to excitation below the cutoff frequency of the first antisymmetric mode. The more dispersive antisymmetric wave mode has a wavelength of 9.5 mm, and the symmetric wave mode has a wavelength of 53.0 mm.

Table 1 Sensor locations

	Coordinate, mm	
	X_1	X_2
PZT 1	177.8	330.2
PZT 2	177.8	177.8
PZT 3	304.8	355.6
PZT 4	355.6	177.8

In the numerical analysis, spatial resolution on numbers of node per minimum wavelength is a key factor to obtaining accurate solutions. The mesh configuration is shown in Fig. 2c. In this case, the 3-D spectral element has $5 \times 5 \times 1$ mm as the maximum size and a fifth-order Lagrange interpolation in the element. The total number of nodes and elements are 1,656,360 and 11,040, respectively. This configuration gives about ten nodes per wavelength along the propagation direction. The reason such resolution is employed will be discussed in Sec. IV. To subdivide the whole domain into elements, as shown in Fig. 2c, the FEM-based commercial code ABAQUS/CAE is used as a preprocessor to discretize the structure. The finite elements created from the preprocessor were transformed into spectral elements through an element-transformation program that was developed during the investigation for the SEM model. As a boundary condition, the plate was assumed to be under a traction-free condition. Furthermore, the excitation in the form of electric voltage was applied to nodal points on the top surface of actuator PZT 2 in steps with respect to time, as shown in Fig. 2b. All calculations were performed using a personal computer: Pentium IV 2.66-GHz CPU, 512-MB RAM, and Compaq Visual Fortran 6.5. It is worth noting

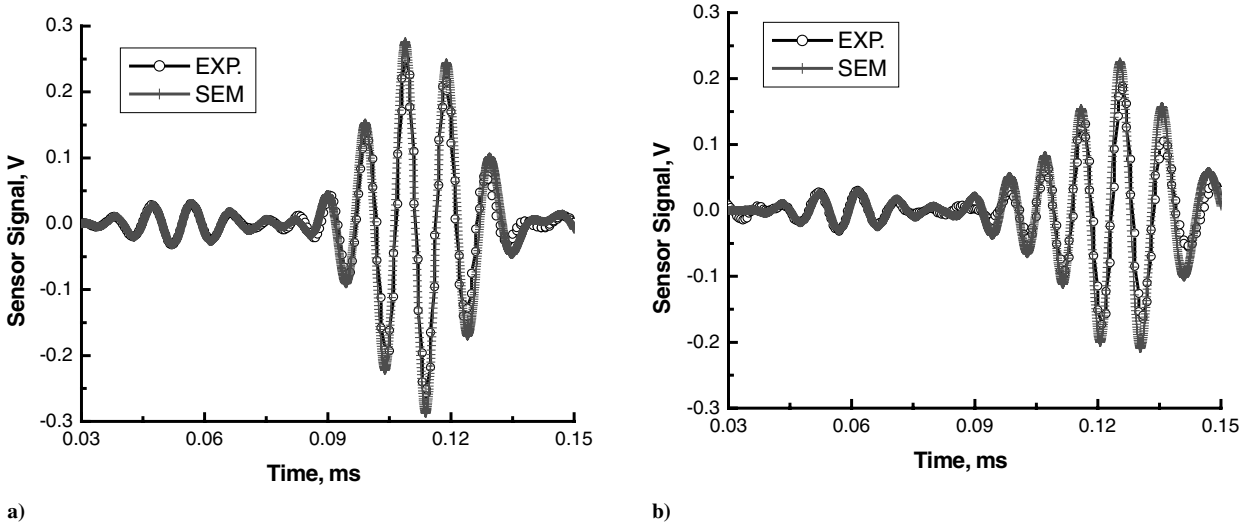

Fig. 3 Sensor signals at a) PZT 1 and b) PZT 4.

that no attempt was initially made to model the thin adhesive layer between the piezoelectric materials and the host aluminum, for which the mechanical properties were quite different from those of either the piezoelectric ceramics or the host aluminum plate.

The proposed SEM method without considering the adhesive layer (perfect bonding) quite accurately simulated the response of sensor measurements in a pitch–catch mode, as shown in Fig. 3 at 100 KHz, in which the measured sensor signals were compared with the simulated results in response to a five-peak wave excitation generated at PZT 2. As previously stated, only two fundamental modes are observed in this figure. Furthermore, the antisymmetric mode with relatively slower velocity and larger signal strength shows more dispersive features, compared with the symmetric mode. The good agreement between experimental results and numerical solutions verifies that the SEM-based code with coupled explicit time-marching and static solving schemes is capable of simultaneously solving the coupled electromechanical fields for Lamb wave simulation. In this code, the sensor output as volts is the mean of the nodal voltages obtained from solving the coupled Eqs. (4a) and (4b) on all nodes on the PZT sensor surface.

However, comparisons of the simulation results with signals generated near 400 KHz, which was close to the resonance frequency of the adhesively bonded piezoelectric ceramic disc, were not as good as those at the lower frequencies: particularly, the wave amplitude and the number of peaks (see Sec. VI). Meshes were further refined on the plate, but there was no significant improvement in the calculation. This led to a conclusion that the adhesive layer might have played a role in influencing the energy transmission from the piezoelectric actuator to the host structures. Therefore, a study of the effect of the adhesive layer on the Lamb wave generation was performed and the results will be presented in the last section of the paper. The efficiency and accuracy of the proposed SEM method will be discussed in the next section.

IV. Performance and Efficiency

To study the efficiency and accuracy of the spectral element analysis for ultrasonic Lamb wave propagation, the solution convergence rate through the increase of the spatial resolution is examined by comparing with a finite element code that was developed by the authors during the course of the study. Both the FEM and SEM codes employ the same algorithm of solving the coupled electromechanical field equations (unfortunately, no commercial codes can provide such a comparison). The only difference between the two codes is the fact that the SEM uses various high-order interpolations and GLL quadrature, whereas the FEM is based on linear interpolation and the usual Gauss quadrature, as discussed in Sec. II. Thus, decreasing the finite element size is the only way to improve the spatial resolution, whereas, in addition to decreasing spectral element size, the use of higher-order interpolation enhances the resolution. Furthermore, there are two integration schemes in FEM. In the context of computational cost, a reduced-integration scheme for explicit FEM is a better choice than full integration. In contrast, the full-integration scheme is better than the reduced-integration scheme in terms of solution accuracy [11]. In this study, both reduced- and full-integration schemes are employed to investigate the two aspects of efficiency and accuracy.

As a test model, a thin aluminum plate with two surface-mounted piezoelectric transducers was considered, as illustrated in Fig. 4a. The thin plate has a sufficiently large dimension in the X_2 direction compared with the dimensions in the X_1 and X_3 direction ($508 \times \infty \times 1.02$ mm). The piezoelectric transducers with X_3 poling direction are running parallel to the X_2 direction ($6.35 \times \infty \times 0.25$ mm). Therefore, this example can be considered to be in the state of plane strain deformation under uniform voltage input on the transducer upper surface, wherein the displacement in the X_2 axis disappears identically to zero. This simplification makes it easy to examine the effect of spatial resolution in numerical methods without loss of generality. Typical mesh configurations of FEM and SEM for the plane strain problem are shown in Figs. 4b and 4c. For the sake of visualization, the figures are enlarged near one piezoelectric transducer. Furthermore, the SEM-based and FEM-based codes have only a three-dimensional element. To embody the plane strain state using the 3-D element, a very thin element dimension along the X_2 direction is assumed and all X_2 direction degrees of freedom are constrained. Using one of two piezoelectric transducers as an actuator, we excite a five-peak tone-burst wave with a center frequency of 100 kHz, as stated in Sec. III.

The profile of sensor signals is shown in Fig. 5a, in which a smaller-strength symmetric mode is followed by a higher-strength antisymmetric mode. The SEM-based solution is in quantitative accord with FEM-based results. However, in the context of numerical dispersion error, whereas the solutions match almost perfectly for the fundamental symmetric mode, a small discrepancy of phase/group wave velocities is observed in the slower fundamental antisymmetric mode, as shown in Fig. 5b. To investigate the efficiency and accuracy of numerical methods, the discrepancy versus the spatial resolution is examined from quantitative viewpoints, as shown in Fig. 6. In this figure, the SEM exhibits an exponential convergence rate, compared with the FEM. In terms of the solution convergence, the SEM has an excellent advantage over the FEM in simulation of the ultrasonic Lamb wave propagation. Furthermore, as shown in this figure, reduced-integration-based FEM underestimates the group velocity, and full-integration-based FEM overestimates it. Both FEM solutions

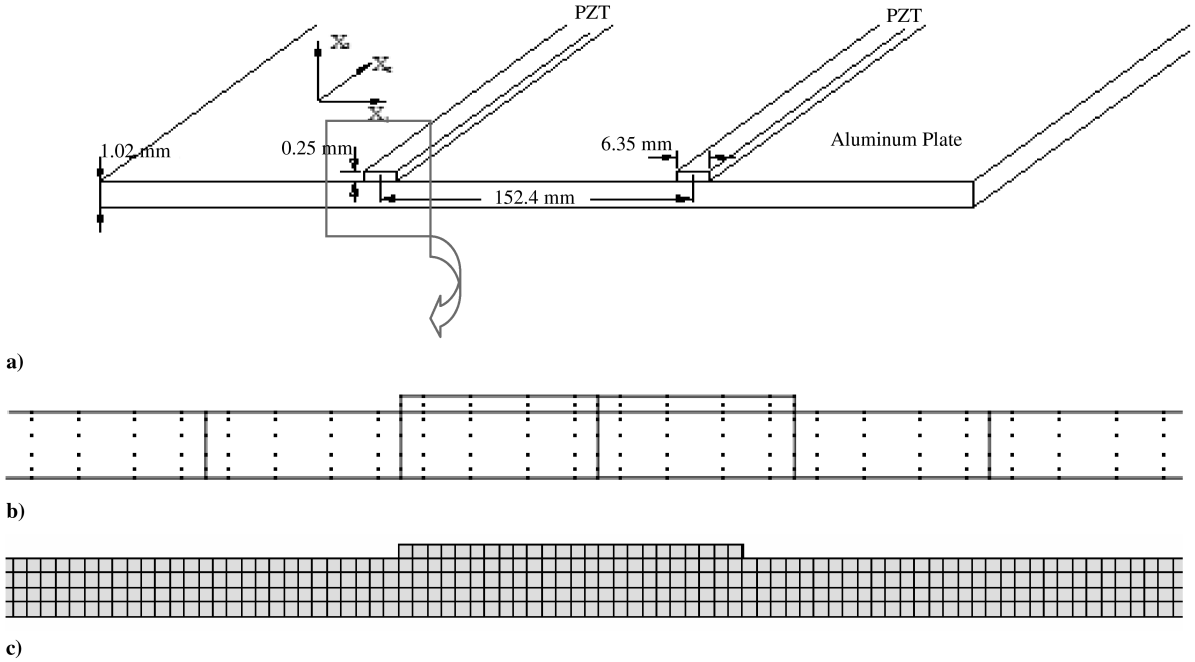

Fig. 4 Configuration of geometry and mesh to study the code performance: a) geometric configuration, b) mesh configuration for finite element analysis, and c) mesh configuration for spectral element analysis.

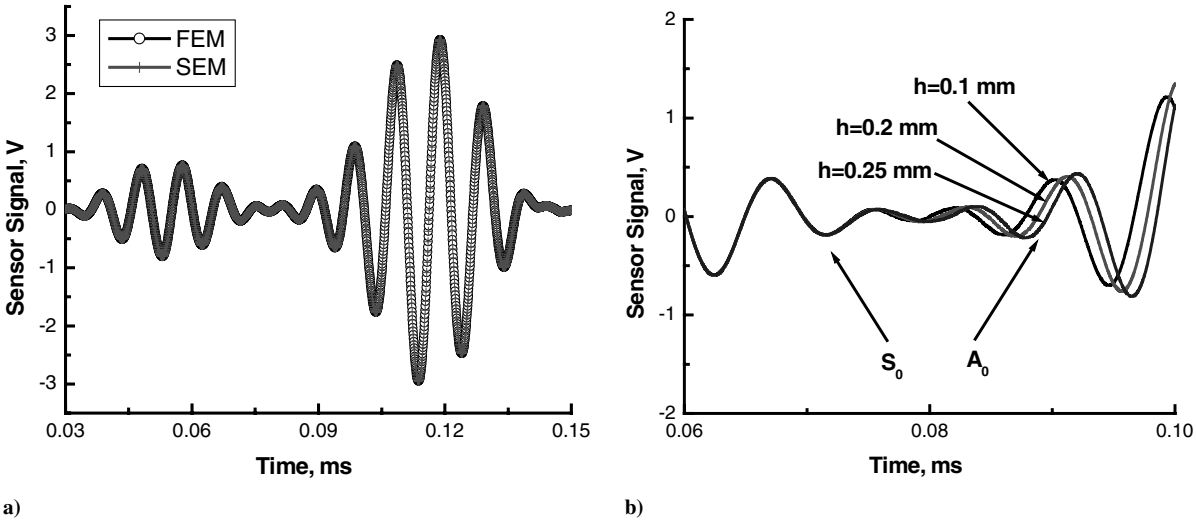

Fig. 5 Sensor signals a) comparison between FEM and SEM and b) error of wave velocity in FEM.

asymptotically converge to a solution as the resolution increases. The solution as the element size goes to zero ($h \to 0$) is easily calculated by Richardson extrapolation [22]. According to the mathematical approach for FEM [23], the numerical dispersion error in linear FEM decreases with h^2. Under the assumption of asymptotic error expansion, the improved solution of the arrival time obtained from finite element analysis is calculated as follows:

$$Y(0) = \frac{4Y(h/2) - Y(h)}{3} + O(h^p), \qquad p > 2 \tag{5}$$

For full integration,

$$Y(h) = 115.88 \qquad Y(h/2) = 116.30 \Rightarrow Y(0) = 116.44$$

For reduced integration,

$$Y(h) = 116.65 \qquad Y(h/2) = 117.280 \Rightarrow Y(0) = 116.44$$

The solution accuracy of SEM and FEM is estimated on the basis of the value shown in Table 2. To obtain a solution with less than 0.5%

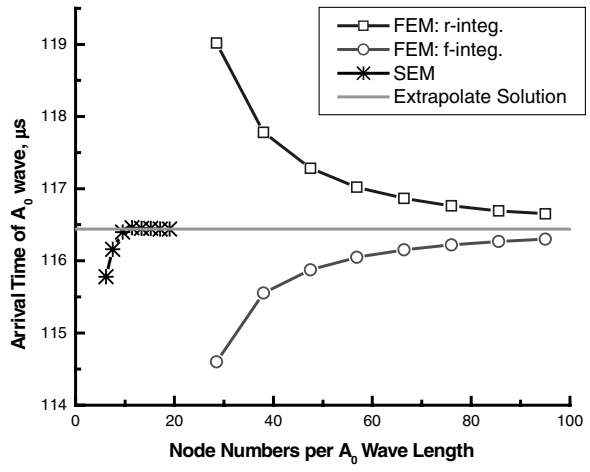

Fig. 6 Solution convergence.

Table 2 Comparison of solution accuracy

SEM		FEM		
Resolution		Resolution	Full integration	Reduced integration
19	116.44 (0.00%)	95	116.30 (0.12%)	116.65 (0.18%)
15	116.45 (0.01%)	76	116.22 (0.19%)	116.76 (0.27%)
11	116.46 (0.03%)	48	115.88 (0.48%)	117.28 (0.72%)
9	116.40 (0.04%)	38	115.55 (0.76%)	117.78 (1.15%)

Table 3 Comparison of computational resources

	SEM	FEM reduced integration
Total number of active DOF	6768	224,648
Computational time	250 s	4280 s

dispersive error, the FEM requires more than 40 nodes per minimum wavelength. Table 3 shows the comparison of computational resources. The SEM reduces the computational memory by more than a factor of 20 in terms of total nodal numbers, compared with the FEM. Furthermore, the FEM costs more than 10 times the computational time, compared with the SEM.

V. Damage-Detection Simulation

To monitor the scattered Lamb wave induced by the crack, a damage-detection procedure using a typical pitch–catch and pulse-echo method is performed with the aid of the proposed SEM method. Consider the same aluminum plate, as previously mentioned in Sec. III. In addition, the plate has a through-thickness circular hole (center at $X_1 = 237$ mm and $X_2 = 279$ mm; 10-mm diameter) and a through-thickness crack (4, 8, or 12 mm) originating from the hole edge, as seen in Fig. 7a. The Lamb wave sensitivity to cracks strongly depends on the excitation frequency. A five-cycle tone-burst waveform with a driving center frequency of 450 kHz is used for the actuation signal, as shown in Fig. 7b. In this frequency range, the symmetric Lamb wave mode, which is more sensitive to the presence of through-thickness cracks in isotropic structures than the

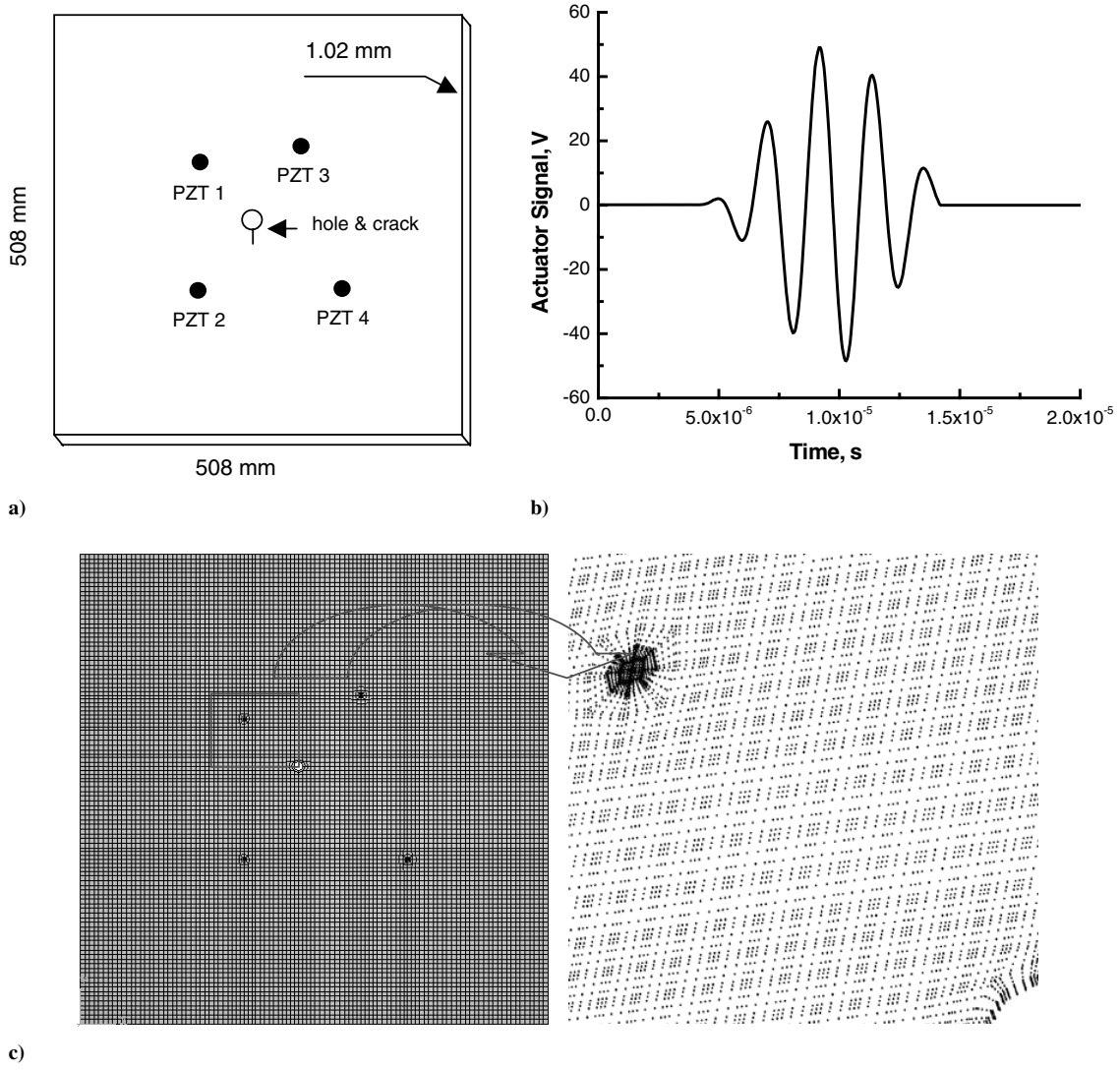

Fig. 7 Square aluminum plate with hole/crack and four piezoelectric transducers on one side a) geometric configuration, b) excitation signal (450 kHz), and c) mesh configuration elements and nodes.

antisymmetric wave mode [3,4], has a much higher amplitude than the antisymmetric mode. Furthermore, the wavelength of the symmetric mode is about 12 mm, which is sensitive enough to detect 4-mm cracks. A typical mesh configuration is shown in Fig. 7c. The maximum 3-D element size is $5 \times 5 \times 1$ mm. In addition, the Lagrange interpolant in each element is fifth order. According to the discussion in Sec. IV, in terms of the symmetric wave mode, this nodal resolution reduces the dispersion error to under 0.05%. The total number of nodes and elements are 1,671,720 and 11,141, respectively.

The proposed SEM method can also be used to simulate the pulse-echo mode, in addition to the typical pitch–catch mode. In terms of the pulse-echo algorithm, the programmed electric voltage first excites a PZT actuator, and then the function as an actuator is artificially stopped at a fixed time step. Also, the element as a sensor starts sensing a reflected wave from damage and boundaries. Figure 8a shows the sensor signals based on the pitch–catch method when PZT 2 and PZT 4 are used as an actuator and sensor, respectively. The first-arrival symmetric wave mode shows higher signal strength than with the antisymmetric wave mode. In terms of the symmetric wave mode, this driving frequency greatly enhances the signal-to-noise ratio, compared with the case of 100-kHz center frequency, as shown in Fig. 3. Figure 8b is the sensor signal when PZT 2 and PZT 4 are used as an actuator/sensor, respectively, based on the pulse-echo method. The time of flight of the first/second arrival waves confirms that it is a symmetric wave mode originating from the hole/crack and plate edge, respectively.

To clearly identify only the scatter waves induced by the crack, both wave-propagation simulations for the plate (shown in Fig. 7) with and without the crack are performed and the results are numerically subtracted. Figure 9a describes the forward-scattered signals obtained from path PZT 2–PZT 3. The scattered signal strength induced at a relatively longer crack is higher. Furthermore, there is no phase shift in the first-arrival scattered signals because the crack is located at a short distance from the direct wave path. Figure 9b shows the simulation result of the scattered wave due to a crack when PZT 2 is used as a pulse-echo element. The scattered waves, which arrive faster as the crack length increases, confirm that it originates from a crack.

The wave developments at different time frames in the model with an 8-mm crack are shown in Fig. 10. To visualize the wave generation and propagation, a graphic interface program is used, which transfers the SEM-based output solution into the input data for the commercial software Tecplot. It is shown that the symmetric and antisymmetric waves were generated at the PZT 2 actuator and propagated outward. These figures show the symmetric waves partially reflected and transmitted to the backward and forward directions, respectively, after the first arrival at the hole/crack. Furthermore, the faster symmetric waves reflected at the plate boundary were mixed with the slower antisymmetric waves. The

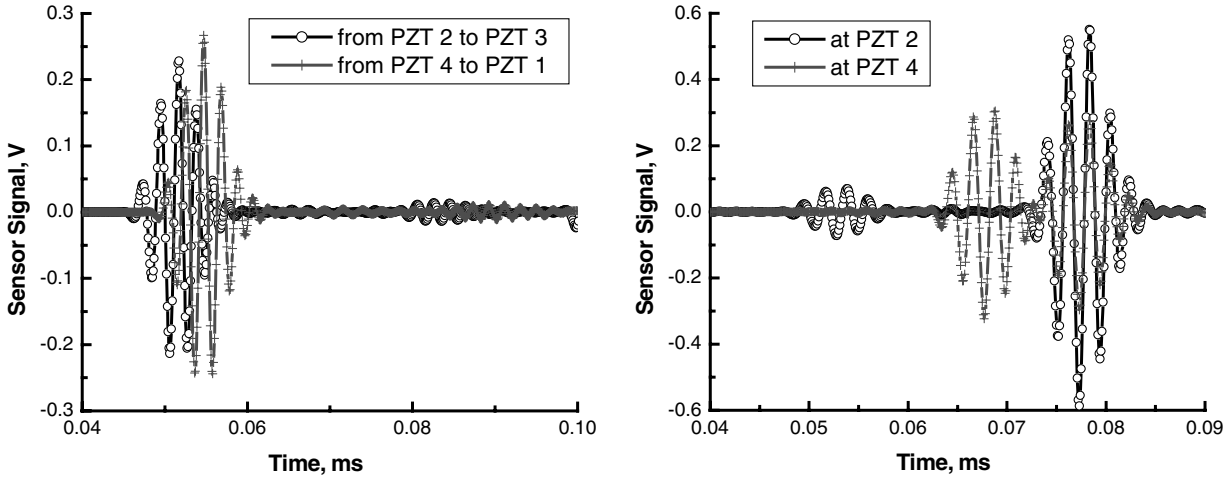

a) b)

Fig. 8 Sensor signals obtained from a) pitch–catch method and b) pulse-echo method.

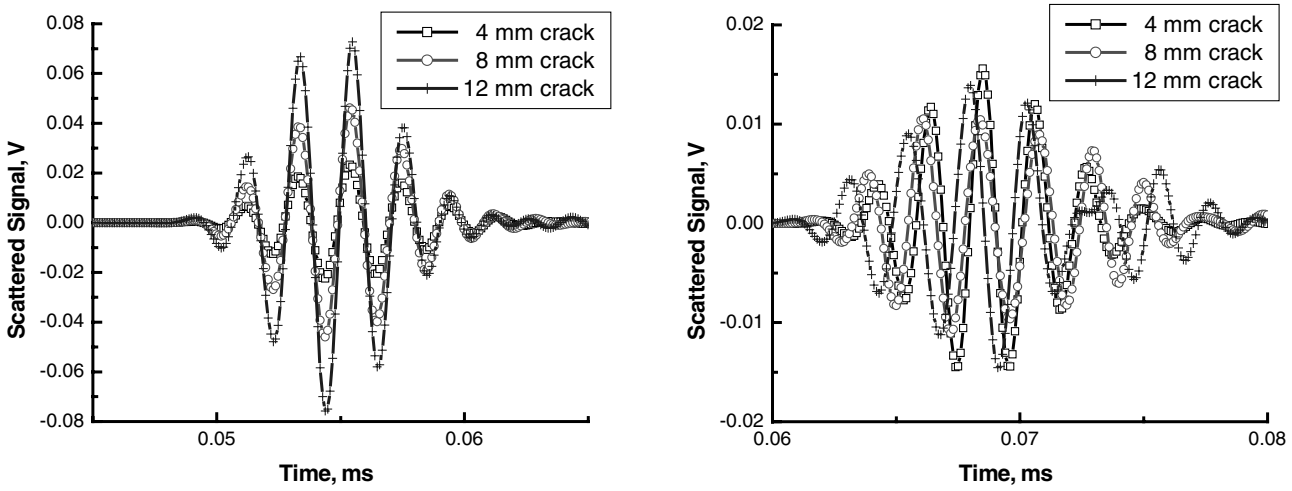

a) b)

Fig. 9 Scatter signals of a) pitch–catch from PZT 4 to PZT 1 and b) pulse-echo at PZT 4.

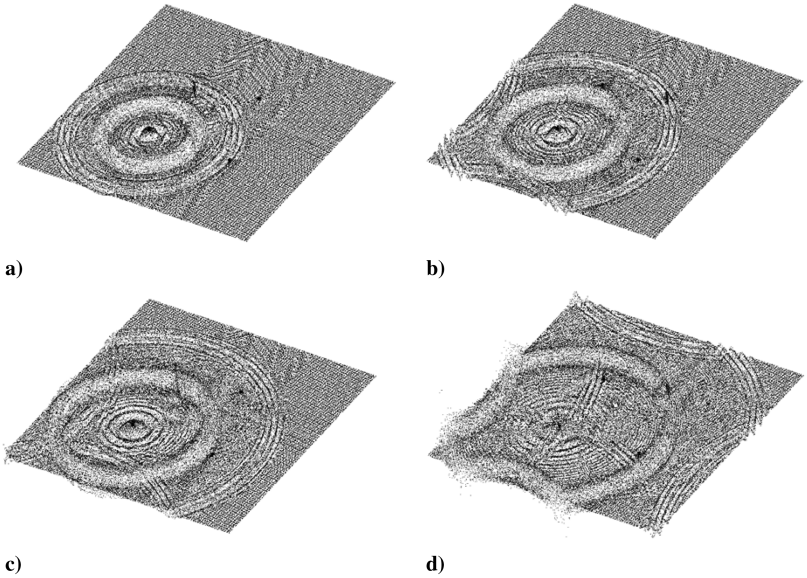

Fig. 10 Wave developments at a) 40 μs, b) 50 μs, c) 60 μs, and d) 80 μs.

wave mixtures induced the complicated wave development as time progressed. Figure 11 shows only the propagating scattered waves from the crack tip at 20 μs and the scattered wave propagating to neighboring sensors at a later time. To easily observe the scattering at the crack, Fig. 11a is enlarged near the hole. These figures clearly show that the scattered signal is induced at the crack, as mentioned earlier. This offers the potential ability of this SEM-based method to detect damage. Furthermore, the SEM method could be used to

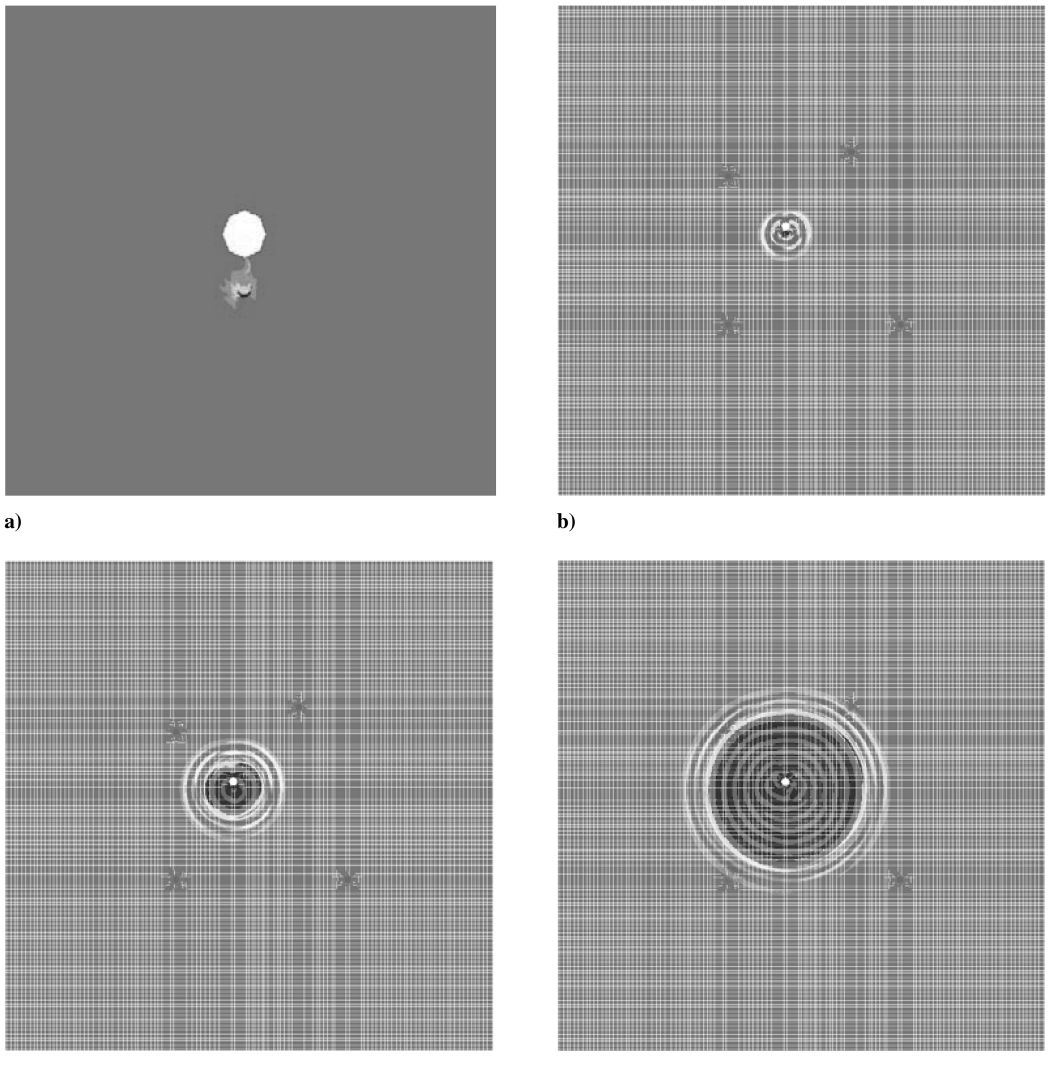

Fig. 11 Scatter wave developments at a) 20 μs, b) 25 μs, c) 30 μs, and d) 40 μs.

optimize key parameters such as sensor shape, size, locations, and input diagnostic waveform to achieve the maximum damage-detection capability with a minimal number of sensors.

VI. Interfacial-Adhesive-Layer Effect

In Sec. III, the SEM code was verified without modeling an interface adhesive layer at an excitation frequency of 100 kHz, which is much lower than the resonant frequency of piezoelectric transducers adhesively bonded to an aluminum plate. As an excitation frequency approaches the resonant frequency, the effects of the adhesive layer become more prominent. Figure 12 shows the SEM simulation and an experimental result at 400-kHz excitation with the same configuration as Fig. 3a. The experimental sensor signal has larger amplitude and more peaks compared with the SEM simulation. It seems that the interfacial adhesive property relative to the properties of piezoelectric actuators and sensors near the resonant frequency plays an important role on the response of the structure.

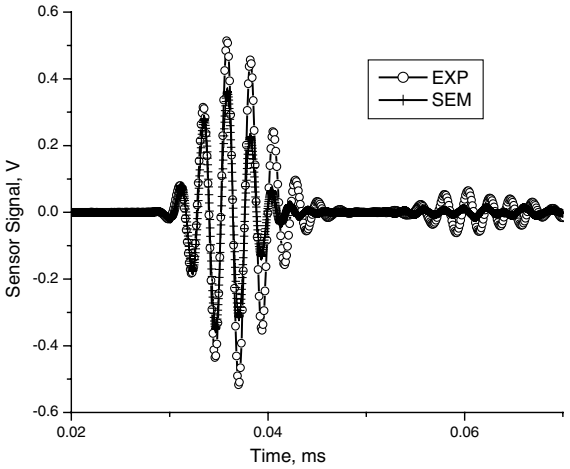

Fig. 12 Sensor signals at PZT 1 (refer to Fig. 2) with 400-kHz excitation.

To model the interfacial adhesive, a much finer mesh will be required for a 3-D analysis, which is prohibitive for this study. Instead, a 2-D plane strain model was developed, as shown in Fig. 13 for the thin adhesive layer, to simplify the problem. The 2-D model has the same propagation distance and piezoelectric transducer diameter as the 3-D model. A model without adhesive is compared with a model with a 50-μm adhesive layer. As the thickness of the adhesive layer increases, larger amplitude and more peaks occur in both symmetric (S0) and antisymmetric (A0) mode, similar to the 3-D results shown in Fig. 12. From this study, it is inferred that the existence of the adhesive layer lowers the resonance frequency and makes it closer to the 400-kHz excitation frequency. As a result, resonant effects such as larger amplitude and more peaks appear. Also, the result of the simulations turned out to be very consistent with the recent tests that were conducted to study the effect of adhesive-layer thickness on the Lamb wave excitation and propagation in structures [24]. Therefore, it is recommended that a further study on adhesive-layer modeling is required to simulate wave propagation with an excitation close to the resonant frequency of a piezoelectric transducer adhesively bonded to a structure.

VII. Conclusions

An SEM-based computational method was developed for modeling the outputs of a built-in piezoelectric sensor in response to an excitation induced by a built-in piezoelectric transducer in acousto-ultrasound range on a metallic structure integrated with a network of piezoelectric transducers and sensors. The method solves a coupled electromechanical field of equations and employs an explicit time-integration scheme for the elastodynamic solver and Gauss elimination for static electric fields. Based on the study, the following conclusions can be made:

1) The SEM has significant advantages over the FEM in modeling acousto-ultrasonic Lamb wave propagation in terms of computational time and memory space.

2) The proposed SEM method could be used to directly study the sensitivity of sensor signals to damage in platelike structures by controlling the electrical excitation waveform to the piezoelectric transducer.

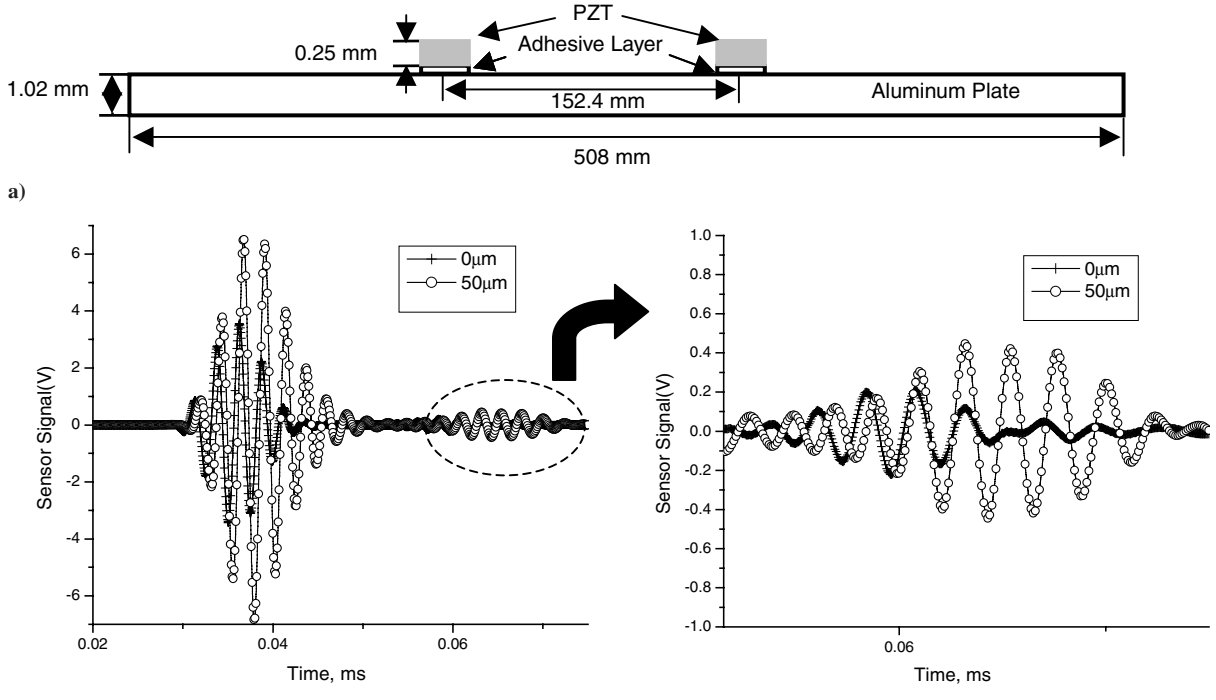

Fig. 13 Two-dimensional adhesive-layer model: a) two-dimensional plain strain model configuration, b) sensor signal at 400-kHz excitation for adhesive-layer-thickness models (left) and A0 mode (right).

3) The proposed SEM method could also be used to study the sensor and actuator placement for a particular structure to optimize the sensor output sensitivity.

4) A more efficient and effective method is needed to study the dynamic behavior of the adhesive interface near the resonance frequency of the built-in transducer in the acousto-ultrasound excitation range.

Acknowledgments

The authors are grateful for the support of U.S. Air Force Office of Scientific Research (AFOSR) through grant FA9550-04-1-0150 and National Science Foundation (NSF) grant CMS-0-200399. The AFOSR program monitor is Les Lee and NSF program monitor is Shih Chi Liu.

References

[1] Roh, Y. S., and Chang, F. K., "Built-In Diagnostics for Identifying an Anomaly in Plate Using Wave Scattering," Ph.D. Dissertation, Aeronautics and Astronautics Dept., Stanford Univ., Stanford, CA, 1999.

[2] Kessler, S. S., Spearing, S. M., and Soutis, C., "Structural Health Monitoring in Composite Materials Using Lamb Wave Methods," *Smart Materials and Structures*, Vol. 11, Apr. 2002, pp. 269–278. doi:10.1088/0964-1726/11/2/310

[3] Ihn, J. B., and Chang, F. K., "Detection and Monitoring of Hidden Fatigue Crack Growth Using a Built-in Piezoelectric Sensor/Actuator Network, 1: Diagnostics," *Smart Materials and Structures*, Vol. 13, No. 3, 2004, pp. 609–620. doi:10.1088/0964-1726/13/3/020.

[4] Ihn, J. B., and Chang, F. K., "Detection and Monitoring of Hidden Fatigue Crack Growth Using a Built-in Piezoelectric Sensor/Actuator Network, 2: Validation Using Riveted Joints and Repair Patches," *Smart Materials and Structures*, Vol. 13, No. 3, 2004, pp. 621–630. doi:10.1088/0964-1726/13/3/021.

[5] Kehlenbach, M., Kohler, B., Cao, X., and Hanselka, H., "Numerical and Experimental Investigation of Lamb Wave Interaction with Discontinuities," *Proceedings of the 4th International Workshop on Structural Health Monitoring*, edited by Chang, F. K., Stanford Univ., Stanford, CA, 2003, pp. 15–17.

[6] Mackerle, J., "Finite-Element Modelling of Non-Destructive Material Evaluation, an Addendum: A Bibliography (1997–2003)," *Modelling and Simulation in Materials Science and Engineering*, Vol. 12, No. 5, 2004, pp. 799–834. doi:10.1088/0965-0393/12/5/004

[7] Su, Z., "Fundamental Lamb Mode-Based Delamination Detection for CF/EP Composite Laminates Using Distributed Piezoelectrics," *Structural Health Monitoring: SHM*, Vol. 3, No. 1, 2004, pp. 43–68. doi:10.1177/1475921704041874

[8] Lee, B. C., and Staszewski, W. J., "Modeling of Lamb Waves for Damage Detection in Metallic Structures, Part 1: Wave Propagation," *Smart Materials and Structures*, Vol. 12, No. 5, 2003, pp. 804–814. doi:10.1088/0964-1726/12/5/018

[9] Lee, B. C., and Staszewski, W. J., "Modeling of Lamb Waves for Damage Detection in Metallic Structures, Part 2: Wave Interactions with Damage," *Smart Materials and Structures*, Vol. 12, No. 5, 2003, pp. 815–824. doi:10.1088/0964-1726/12/5/019

[10] Cho, Y., Hongerholt, D. D., and Rose, J. L., "Lamb Wave Scattering Analysis for Reflector Characterization," *IEEE Transactions on Ultrasonics, Ferroelectrics and Frequency Control*, Vol. 44, No. 1, 1997, pp. 44–52. doi:10.1109/58.585189

[11] Mullen, R., and Belytschko, T., "Dispersion Analysis of Finite Element Semidiscretizations of the Two-Dimensional Wave Equation," *International Journal of Numerical Methods in Engineering*, Vol. 18, No. 1, 1982, pp. 11–29. doi:10.1002/nme.1620180103

[12] Patera, A. T., "A Spectral Element Method for Fluid Dynamics: Lamina Flow in a Channel Expansion," *Journal of Computational Physics*, Vol. 54, June 1984, pp. 468–488. doi:10.1016/0021-9991(84)90128-1

[13] Dauksher, W., and Emery, A. F., "An Evaluation of the Cost Effectiveness of Chebyshev Spectral and P-Finite Element Solutions to the Scalar Wave Equation," *International Journal of Numerical Methods in Engineering*, Vol. 45, No. 8, 1999, pp. 1099–1113. doi:10.1002/(SICI)1097-0207(19990720)45:8<1099::AID-NME622>3.0.CO;2-5

[14] Priolo, R. G., Carcione, J. M., and Seriani, G., "Numerical Simulation of Interface Waves by High-Order Spectral Modeling Techniques," *Journal of the Acoustical Society of America*, Vol. 95, No. 2, 1994, pp. 681–693. doi:10.1121/1.408428

[15] Seriani, G., and Priolo, E., "Spectral Element Method for Acoustic Wave Simulation in Heterogeneous Media," *Finite Elements in Analysis and Design*, Vol. 16, Nos. 3–4, 1994, pp. 337–348. doi:10.1016/0168-874X(94)90076-0

[16] Komatitsch, D., and Vilotte, J. P., "The Spectral Element Method: An Efficient Tool to Simulate the Seismic Response of 2-D and 3-D Geological Structures," *Bulletin of the Seismological Society of America*, Vol. 88, No. 2, 1998, pp. 368–392.

[17] Komatitsch, D., Barnes, C., and Tromp, J., "Simulation of Anisotropic Wave Propagation Based Upon A Spectral Element Method," *Geophysics*, Vol. 65, No. 4, 2000, pp. 1251–1260. doi:10.1190/1.1444816

[18] Ostachowicz, W., Krawczuk, M., Cartmell, M., and Gilchrist, M., "Wave Propagation in Delaminated Beam," *Computers and Structures*, Vol. 82, No. 6, 2004, pp. 475–483. doi:10.1016/j.compstruc.2003.11.001

[19] Doyle, J. F., *Wave Propagation in Structures*, Springer–Verlag, New York, 1997.

[20] Hughes, T. J. R., *The Finite Element Method: Linear Static and Dynamic Finite Element Analysis*, Prentice–Hall, Englewood Cliffs, NJ, 1987.

[21] Ha, S. K., Keilers, C., and Chang, F. K., "Finite Element Analysis of Composite Structures Containing Distributed Piezoceramic Sensors and Actuators," *AIAA Journal*, Vol. 30, No. 3, 1992, pp. 772–780.

[22] Roache, P. J., "Quantification of Uncertainty in Computational Fluid Dynamics," *Annual Review of Fluid Mechanics*, Vol. 29, Jan. 1997, pp. 123–160. doi:10.1146/annurev.fluid.29.1.123

[23] Ihlenburg, F., and Babuska, I., "Finite Element Solution of the Helmholtz Equation with High Wave Number, Part 2: The *h-p* Version of the FEM," *SIAM Journal on Numerical Analysis*, Vol. 34, No. 1, 1997, pp. 315–358. doi:10.1137/S0036142994272337

[24] Lanzara, G., Yoon, Y., and Chang, F.-K., "Multifunctional Piezoelectric Actuators with Carbon Nanotube Films," *Structural Health Monitoring: SHM* (submitted for publication).

M. Ahmadian
Associate Editor